


Drag and lift coefficients of ellipsoidal particles under rarefied flow conditionsC. Livi¹, G. Di Staso^{1,2}, H. J. H. Clercx¹, and F. Toschi^{1,3}¹*Fluids and Flows Group and J.M. Burgers Centre for Fluid Dynamics, Department of Applied Physics, Eindhoven University of Technology, P.O. Box 513, 5600MB Eindhoven, The Netherlands*²*FLOW Matters Consultancy B.V., Groene Loper 5, 5612AE Eindhoven, The Netherlands*³*CNR-IAC, I-00185 Rome, Italy* (Received 7 July 2021; accepted 20 December 2021; published 13 January 2022; corrected 3 August 2022)

The capability to simulate a two-way coupled interaction between a rarefied gas and an arbitrary-shaped colloidal particle is important for many practical applications, such as aerospace engineering, lung drug delivery, and semiconductor manufacturing. By means of numerical simulations based on the direct-simulation Monte Carlo (DSMC) method, we investigate the influence of the orientation of the particle and rarefaction on the drag and lift coefficients, in the case of prolate and oblate ellipsoidal particles immersed in a uniform ambient flow. This is done by modeling the solid particles using a cut-cell algorithm embedded within our DSMC solver. In this approach, the surface of the particle is described by its analytical expression and the microscopic gas-solid interactions are computed exactly using a ray-tracing technique. The measured drag and lift coefficients are used to extend the correlations, based on the sine-squared drag law, available in the continuum regime to the rarefied regime, focusing on the transitional and free-molecular regimes. The functional forms of the correlations for the ellipsoidal particles are chosen as a generalization from the spherical case. We show that the fits over the data from numerical simulations can be extended to regimes outside the simulated range of Kn. Our approach allows to achieve a higher precision when compared with existing predictive models from the literature. Finally, we underline the importance of this work in providing correlations for nonspherical particles that can be used for point-particle Euler-Lagrangian simulations to address the problem of contamination from finite-size particles in high-tech mechanical systems.

DOI: [10.1103/PhysRevE.105.015306](https://doi.org/10.1103/PhysRevE.105.015306)**I. INTRODUCTION**

Multiphase flows including particulate suspensions in conditions where the flow around the particles is rarefied are important in many different natural, medical, and industrial applications. Examples can be found in the formation of cloud droplets and in ozone depletion in the stratosphere [1], contamination from particle debris in high-tech mechanical systems [2], and lung drug delivery [3]. In all these cases the typical size of the particles is small when compared to the mean free path of the surrounding gas molecules and rarefaction effects are important in gas-surface interactions.

Numerous studies have been proposed to address the problem of shape influence on the transport of particles in the continuum regime. From the pioneering theoretical work of Oberbeck [4] and Jeffery [5], who first investigated the motion of an ellipsoid immersed in a fluid in the Stokes limit, an increasingly growing effort has been dedicated to understand shape and orientation effects on the drag, lift, and torque experienced by particles in different flow conditions [6–14].

While the understanding of particle-flow interactions in the continuum regime is consistently increasing through the years, our knowledge on the impact of rarefaction on the dynamics of the particles is still limited. From the numerical point of view, limitations arise as Navier-Stokes solvers fail due to the breakdown of the continuum assumption, while

from the experimental point of view it is difficult to create ideal conditions to investigate the dynamics of very small particles in low-pressure environments.

Typically, Eulerian-Lagrangian simulations are employed in numerical studies related to the transport of nanosized particles in micromechanical devices [15–19]. In this approach, the flow field is evaluated on Eulerian grids, while the solid bodies are modeled as (spherical) point particles and evolved in time in a Lagrangian fashion. Rarefaction effects are then included through the phenomenological Cunningham corrections [20,21] on the drag force experienced by the particles. Although, in general, this approach is a reasonable approximation for the dynamics of micro- and nanometric particles immersed in a gas, any effect related to their finite size, shape, and orientation is neglected. Such effects are essential in high-tech applications, where high accuracy is required in the modeling approach, so that finite-size effects must often be taken into account.

Different authors addressed, both analytically and numerically, the interaction between rarefied gas flows and a finite-size spherical particle. Epstein [22] first derived a drag relation for a sphere translating in a gas at thermal equilibrium in the free-molecular regime in the limit of low velocities. This approach was later extended by Baines *et al.* [23] to account for larger velocities. Gallis *et al.* [24,25] proposed a formulation based on the use of the Green's function to calculate drag and heat flux experienced by a sphere

in the free-molecular regime for monatomic and diatomic gases.

While the aforementioned analyses are focused on the free-molecular regime, Phillips [26] provided an analytical expression for the drag force on a sphere through an approximate solution of the Boltzmann equation which includes the effects of intermolecular collisions. His approach, based on the method of moments [27,28], is applicable to a large range of Knudsen numbers, covering the slip and transition regimes ($0.0865 \leq \text{Kn} \leq 3.36$). The results from Phillips show a good match with the experimental observations from Millikan [29,30]. These approaches are, however, limited to spherical particles and have not been extended, so far, to particles with more complex shapes.

Some works are available in the literature that tackle the problem of gas-solid interactions in the case of nonspherical particles from a theoretical perspective: Halbritter [31] derived a formulation for the torque exerted by a rarefied gas on an ellipsoidal particle at thermal equilibrium. Dahneke [32] extended the analytical formulation from Epstein to particles with different shapes, including cylinders, and prolate and oblate ellipsoids. These studies are again limited to free-molecular flows.

Some phenomenological models have been proposed [33] to describe the drag corrections experienced by nonspherical particles in the transition and slip flow regimes, such as the equivalent sphere approximation (ESA) and the adjusted sphere approximation (ASA). As it will be further explained later, these approaches are based on the approximation of the investigated particle with an appropriate spherical volume, and rarefaction effects are included through the Cunningham corrections. The main feature of the ASA model is that it retains orientation effects, but it requires the knowledge of the drag force on the body in the continuum and free-molecular regimes, and this information is only available for a limited number of shapes.

To numerically address rarefied gas flow problems in a broad spectrum of Kn, ranging from slip to free-molecular flows, the direct-simulation Monte Carlo (DSMC) method [34,35] has proven to be a stable and accurate approach to accurately model the Boltzmann equation [36,37]. We employ the DSMC method due to its versatility in including solid particles with different shapes in the simulation domain, combined with its capability to correctly describe rarefaction effects and gas-surface interactions. Two main approaches are usually applied to model the surface of the particle in the DSMC framework: In one case, it is approximated by a non-Cartesian body-fitted mesh, and every face on the meshed surface coincides with a DSMC grid cell face on the gas domain [38]. In the second approach, the surface of the particle is represented with its analytical expression and it is free to move on the Cartesian DSMC grid.

The latter approach, first introduced in 1999 by LeBeau [39], has been called the cut-cell method [40,41], as the superimposition of the solid particle volume on the DSMC Cartesian grid imposes that some of the DSMC grid cells (i.e., the boundary cells at the gas-solid interface) are cut by the solid surface, requiring to dynamically compute and update the volume of such cells. The cut-cell method provides two main advantages: it allows to describe the surface of the

particle analytically and, when the motion of the particle is present, it overcomes the need of adaptive remeshing of the simulation grid at every time step, as only the cut-cell volumes have to be recomputed.

Examples of recent successful applications of the cut-cell method to model gas-particle interactions can be found in the literature. Jin *et al.* [42] proposed an efficient approach to recalculate the cut-cell volume based on a polyhedral approximation of the solid volume fraction in each boundary cell. They applied this approach to spherical particles as well as to particles with more complex surfaces. Shrestha *et al.* [43] applied the cut-cell algorithm to study the Brownian diffusion of a spherical particle in the free-molecular regime and the transport of an arbitrary-shaped particle driven by the thermophoretic force. In their formulation the surface of the particle is approximated by a triangulated mesh. Baier *et al.* [44] investigated the thermophoretic force experienced by spherical Janus particles in presence of an external thermal gradient. Chinnappan *et al.* [45] addressed the transport dynamics of ellipsoidal particles in the free-molecular gas flow regime. The aforementioned studies are focused on the free-molecular regime and, up to our knowledge, an extensive investigation of the drag and lift correlations in the transitional regime is still missing in the literature.

In this work we cover this gap by addressing the impact of a finite Knudsen number ($1 \leq \text{Kn} \leq 10$) in the interactions between a gas flow and ellipsoidal particles. This range of Knudsen number is particularly relevant for modern industrial problems, as most of the gas flows are not in the free-molecular regime, although still at very low pressure, and the Knudsen number based on the particle size of the contaminant particles often exceeds unity. To efficiently investigate gas-solid interactions at lower values of Knudsen number ($\text{Kn} < 1$), where the DSMC simulations may become very expensive, alternative techniques can be employed, such as the method of moments [26,46] or appropriate lattice Boltzmann models [47,48].

We propose a cut-cell algorithm which is able to describe a spheroidal particle exactly, at any aspect ratio. Through the use of a modified ray-sphere intersection approach, the collision points between the gas molecules and the ellipsoidal solid particle are obtained at the exact position on the surface of the particle and the volume of the boundary cells (cut cells) is computed through a Monte Carlo approach. This approach differs from both the triangulated approximation of the surface of the solid body proposed in [40,41,43,49] and the polyhedral approximation of the cut cells proposed in [42]. In particular, when compared with modern state-of-the-art, multipurpose DSMC algorithms [40,49], in which solid surfaces are approximated through a triangulated surface mesh and cut-cell volume evaluated through a cut or split algorithm [40], our approach allows to describe the surface of spheroidal particles via their analytical representation, limiting numerical approximations only to the evaluation of the cut cells' volume. This requires that surfaces can be represented mathematically, and for the more general case of arbitrary-shaped surfaces a generalized approach such as the one discussed in Appendix A or the one used in [40,49] is required.

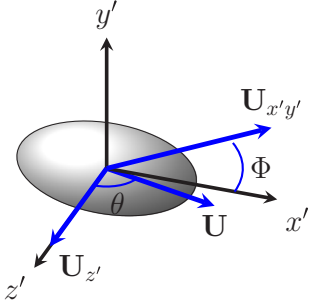


FIG. 1. Sketch of an ellipsoidal particle immersed in a uniform Stokes flow with velocity \mathbf{U} for an arbitrary orientation. In the body-centered reference, (x', y', z') , the ambient velocity \mathbf{U} can be decomposed in its components $\mathbf{U}_{x'y'}$, lying on the $x'y'$ plane forming an angle Φ with respect to the x' axis, and $\mathbf{U}_{z'}$, lying on the z' axis. Since $\mathbf{U}_{z'}$ is independent of the relative orientation between the particle and the flow, orientation effects are described by the angle of attack, Φ , without loss of generality.

We use this algorithm to investigate rarefaction and orientation effects of an impinging uniform gas flow on different ellipsoidal particles. This class of problems can be studied, without loss of generality, by changing the angle of attack at which the gas flow impinges on the simulated particles, as sketched in Fig. 1. We first aim to verify the validity of the sine-squared drag law in the presence of rarefaction. The sine-squared correlation of the drag force experienced by an arbitrary-shaped particle as a function of its orientation was first proposed by Happel and Brenner [50] for Stokes flows in the continuum regime, and later extended by Sanjeevi *et al.* [13,14] to larger Reynolds numbers. Here we plan to investigate and extend its validity in the case of rarefied flows.

We perform this analysis for different Knudsen numbers ranging from the transitional to the free-molecular regime by defining a suitable definition of the Knudsen number for ellipsoidal particles. We first show that the sine-squared drag law typical for the continuum regime is preserved for the whole range of investigated Knudsen numbers, and then we use this correlation to build a heuristic model which is able to predict rarefaction and orientation effects on the hydrodynamic forces acting on the ellipsoidal particles. Such a model can be used to improve existing Euler-Lagrangian simulations of particle transport in rarefied conditions, as it would allow to model ellipsoidal particles and to include orientation effects in the dynamics of the simulated particles.

The paper is structured as follows: In Sec. II we present a detailed analysis and validation of the proposed numerical scheme, showing its capability to recover the drag force exerted by a uniform ambient flow on spherical and ellipsoidal particles in different conditions. In Sec. III we introduce and discuss the definition for the Knudsen number for ellipsoidal particles based on the equivalent sphere, and we show the validity of the sine-squared drag law in the investigated range of Knudsen numbers. In Sec. IV we propose the predictive model for the drag and lift coefficients of a prolate and oblate ellipsoidal particle. We summarize and discuss our results in Sec. V. Finally two Appendices are included to further illustrate the details and performances of the algorithm.

II. NUMERICAL METHOD AND VALIDATION

A. Fluid-solid interactions and the cut-cell method

We approach the solution of the Boltzmann equation using the DSMC method featuring the no-time counter (NTC) collision scheme, as first proposed by Bird [34]. In this framework, we present an algorithm based on the cut-cell method to describe the two-way coupling between the gas flow and a spheroidal solid particle immersed in the DSMC computational domain. The surface of the particle immersed in the gas domain is described by its analytical expression, and the momentum exchange between the gas and the solid particle is computed from the microscopic interactions between the simulated gas molecules and the solid surface. In this way we overcome the limitations of the alternative method used to evaluate the force and the torque on the particle based on the macroscopic stress tensor, which is often less accurate due to the statistical fluctuations of the higher-order macroscopic fields around the particle.

The collision points at which the DSMC molecules impinge on the surface of the solid particle are evaluated exactly using a ray-sphere intersection algorithm [51], extended to include ellipsoidal particles. Details of the algorithm are presented in Appendix A. In very few words, it consists of applying a transformation of the space coordinates that allows to describe the ellipsoidal particle as a sphere with unit radius, whose center coincides with the origin of a new translated reference frame. The trajectories of the DSMC particles are recomputed in the transformed reference frame and the collision points are obtained analytically through the evaluation of the intersections between the new trajectories (lines) and the scaled sphere. The collision point coordinates in the original reference frame are obtained by applying the inverse transformation. A diffuse reflection scheme is then applied to reflect the impinging molecules.

For each DSMC molecule i hitting the surface of the solid particle at position \mathbf{x}_i , with initial momentum \mathbf{p}_i and post-collision momentum \mathbf{p}'_i , the total momentum transferred from the gas to the solid particle within a single time step Δt is evaluated as

$$\Delta \mathbf{p} = \sum_i (\mathbf{p}_i - \mathbf{p}'_i), \quad (1)$$

from which the total force \mathbf{F} and torque \mathbf{T} , exerted on the rigid body, can be directly obtained:

$$\mathbf{F} = \sum_i \left(\frac{\mathbf{p}_i - \mathbf{p}'_i}{\Delta t} \right), \quad (2)$$

$$\mathbf{T} = \sum_i \left[(\mathbf{x}_i - \mathbf{X}) \times \left(\frac{\mathbf{p}_i - \mathbf{p}'_i}{\Delta t} \right) \right], \quad (3)$$

where \mathbf{X} denotes the center of mass of the solid particle. While in this work we will focus on particles that are fixed in space, Eqs. (2) and (3) can be used to update the solid particle translational and angular velocities, position, and orientation.

To connect the physical representation of the simulated particle with the Cartesian DSMC grid, the simulation grid is divided into three regions: gas cells completely filled with gas molecules, solid cells that are completely occupied by the solid particle, and boundary cells (cut cells) that are partially

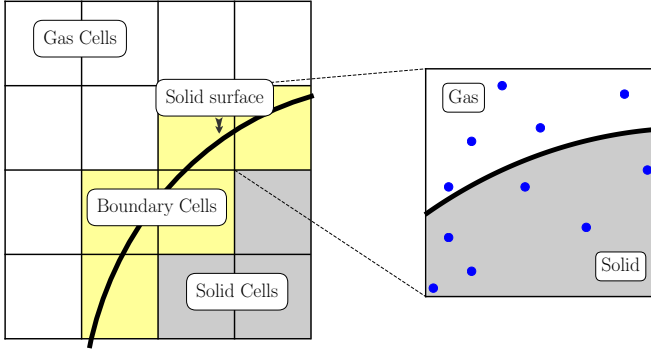


FIG. 2. Sketch of the decomposition of the DSMC computational grid in cells occupied only by the gas (white), cells completely occupied by the solid particle (gray), and boundary cells (yellow) partially occupied by both the gas and the solid. We use a Monte Carlo approach to evaluate the gas and solid volume fractions of the boundary cells.

covered by the solid particle and partially filled with gas, as sketched in Fig. 2. In order to correctly evaluate the intermolecular collisions (and eventually the macroscopic flow fields) within the boundary cells, the local fraction of the cell volume filled with gas has to be calculated. We perform this update by marking the cells close to the solid particle, so that only the marked cells are candidates for being boundary cells. The gas volume of the boundary cells is then evaluated through a Monte Carlo approach: a set of N_t random points is generated in the DSMC boundary cell (blue dots in Fig. 2) and the gas fraction volume, V_g , is obtained as

$$V_g = V_c - V_s = \frac{N_t - N_s}{N_t} V_c, \quad (4)$$

where N_s represents the number of points that are generated inside the solid volume and V_s is the volume fraction of a DSMC cell occupied by the solid volume. The relative error at which the solid volume fraction of the boundary cells is computed can be expressed as [42]

$$\varepsilon_{\text{rel}} = \frac{V_p - \sum_{\text{all cells}} V_s}{V_{p, \text{bound. cells}}}, \quad (5)$$

where V_p is the real (analytic) volume of the solid particle and $V_{p, \text{bound. cells}}$ is the real volume of the solid fraction of all boundary cells.

The scaling of the relative error in Eq. (5), with respect to different resolutions of a spherical particle with radius R (in cell units), is plotted in Fig. 3 for different values of the Monte Carlo trials N_t . It is shown that, using a sufficiently large number of Monte Carlo trials, the volume of the boundary cells is recovered with an accuracy of at least $\sim 95\%$ also for particles with a radius that is smaller than the simulation grid size. Since in this work we only address particles that are fixed in space, the local volume evaluation can be performed only once and we set $N_t = 1 \times 10^5$ to ensure a very high precision of the computation. In cases where the particle is allowed to move, the volume computation must be performed at each time step and a lower number of N_t would allow a faster computation.

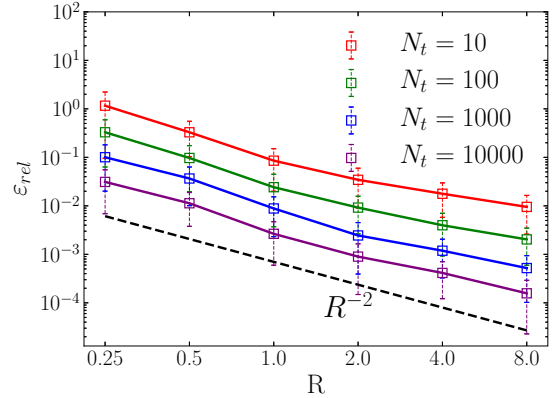


FIG. 3. Relative error ε_{rel} , as defined in Eq. (5), as a function of the radius of the particle, R (cell units), for different values of the Monte Carlo trials N_t . The scaling of the error with respect to the numerical resolution of the particle is second order. The error bars are calculated as the standard deviation calculated on a sample of 100 independent measurements.

B. Drag force measurements validation

To validate the algorithm, we first perform simulations of a rarefied argon gas flow impinging on a spherical particle in the same conditions as [42]. The simulation setup is the following: The radius of the particle is fixed at $R = 0.25 \mu\text{m}$ and the gas temperature is set to $T = 300 \text{ K}$. The gas density ρ , flow velocity U_0 , and pressure P are varied accordingly with the Knudsen number, defined as $\text{Kn} = \lambda/R$, and the (particle-based) Reynolds number, $\text{Re} = 2U_0R/\nu$, is kept constant and equal to 0.022 to match with the setup from [42]. The simulation box size $L = 20R = 5 \mu\text{m}$ to avoid as much as possible detrimental effects due to the vicinity of the particle to the boundaries of the simulation box. Using 120 DSMC cells per linear direction to discretize the domain is sufficient to respect the rule-of-thumb criteria [34,52], ensuring high accuracy for all the simulations. This discretization leads to a particle radius of $R = 6$ (cells units). The number of particles per cell is set to $N_c = 50$, leading to roughly 8.6×10^7 computational particles. Free-streaming boundary conditions are imposed along the flow direction and periodic boundary conditions are applied along the transverse directions. With this configuration we reach a very high accuracy for the investigated range of Kn and, to give an example, for $\text{Kn} = 10$ we have that one computational DSMC particle represents four physical argon atoms.

We validated the proposed algorithm by inspecting the drag force, F_D , experienced by the particles in such a setup for two cases: spherical particles in collisional flows and ellipsoidal particles in collisionless flows. In all the simulations presented in this paper F_D is averaged over $N_{\Delta t} = 10\,000$ time steps after an initial transient of 5000 time steps, which is enough to reach the steady state in all investigated cases. The error bars are calculated using the 95% confidence interval defined as $\varepsilon_{95} = 2\sigma_{\text{std}}/\sqrt{N_{\Delta t}}$, where σ_{std} is the standard deviation on the average value of F_D .

The validation of the drag force experienced by a spherical particle is presented in Fig. 4, where the drag force measured with our DSMC code is compared with the DSMC results

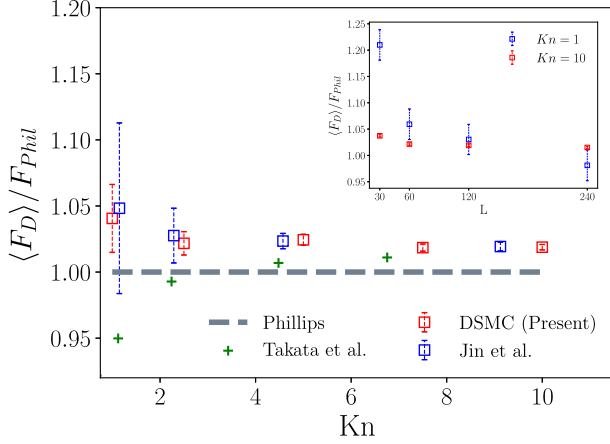


FIG. 4. The average drag force, $\langle F_D \rangle$, on a spherical particle with radius $R = 0.25 \mu\text{m}$ is shown in the main plot as a function of the Knudsen number. Our DSMC simulations (red squares) are compared with the DSMC results from Jin *et al.* [42] (blue squares), and with the analytical approximation from Phillips [26] (gray dashed line) and from Takata *et al.* [53] (green pluses). In the inset, the effects of varying the simulation box size L , leaving all other parameters unchanged, are reported for $Kn = 10$ (red squares) and $Kn = 1$ (blue squares). The error bars are based on ε_{95} .

from Jin *et al.* [42], as well as with the analytical approximations from Takata *et al.* [53] (based on a direct solution of the Boltzmann equation using a finite-difference approach), and Phillips [26] (based on the method of moments developed by Lees [27,28] and extensively described in [46]). The results are normalized with respect to the prediction from Phillips, given by

$$F_{Phil}(R) = -6\pi\mu R U_0 f(Kn), \quad (6)$$

with $f(Kn)$ representing the rarefaction corrections:

$$f(Kn) = \frac{15 - 3c_1 Kn + c_2(8 + \pi\sigma)(c_1^2 + 2)Kn^2}{15 + 12c_1 Kn + 9(c_1^2 + 1)Kn^2 + 18c_2(c_1^2 + 2)Kn^3}, \quad (7)$$

where $c_1 = \frac{2-\sigma}{\sigma}$, $c_2 = \frac{1}{2-\sigma}$, μ is the gas dynamic viscosity, and σ is the momentum accommodation coefficient, with range $0 \leq \sigma \leq 1$. In our simulations $\sigma = 1$ (fully diffusive surface) and thus $c_1 = c_2 = 1$.

As it can be seen from Fig. 4, simulation results with our DSMC method are well aligned with the results available in the literature obtained with similar approaches (see [42]). The consistent small deviation between the values obtained with DSMC solvers and those based on the approximations from Phillips [26] and Takata *et al.* [53] are related to the limitations of the different numerical approaches used in [26,53] to solve the Boltzmann equation. Additionally, the inset shows that setting $L = 120$ is sufficient to exclude detrimental effects due to the finite size of the simulation box.

In the second part of this validation we focus on ellipsoidal particles by comparing results from collisionless simulations with the analytical expressions for the drag force on both prolate and oblate ellipsoidal particles provided by Dahnek  [32]. Dahnek  extended the theoretical approach from Ep-

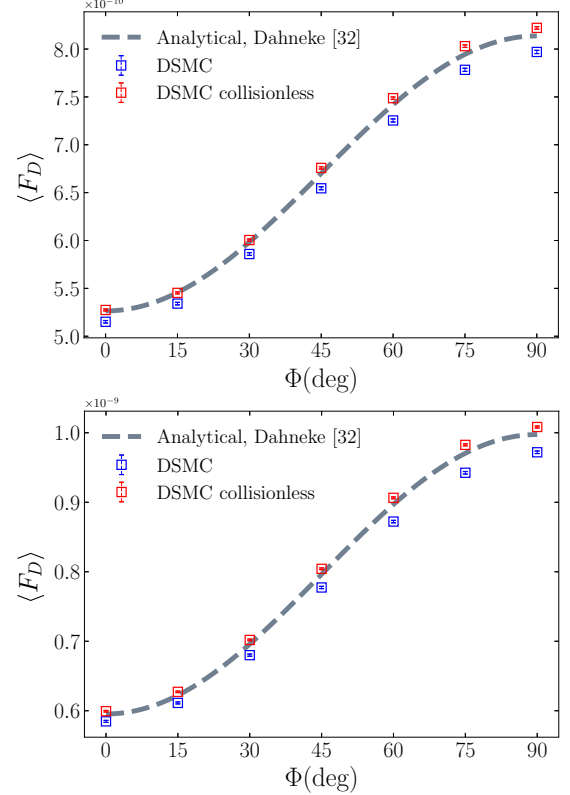


FIG. 5. Drag forces from collisionless DSMC simulations (squares) at $Kn = 10$ for a prolate (top) and oblate (bottom) ellipsoid with aspect ratio $a/b = 2$, for different orientations Φ , are compared with predictions from Dahnek  [32] (gray dashed lines). For completeness, we also present simulation results when intermolecular collisions are present (blue). The error bars are based on ε_{95} .

stein, valid for small streaming velocities, to particles with different shapes, assuming that the reflected gas molecules do not interact with the incoming ones (collisionless limit). We can achieve this in the DSMC simulations by artificially switching off intermolecular collisions. In our simulations we fix the volume of the ellipsoidal particles to the same value as the one used for the spherical particle. The aspect ratio of the ellipsoidal particles is fixed to $a/b = 2$, leading to a major radius $a = 0.39 \mu\text{m}$ for the prolate case and $a = 0.315 \mu\text{m}$ for the oblate case.

Similarly to the spherical case, the physical simulation box size is set in relation to the major radius of the simulated particles, so that $L = 20a = 8 \mu\text{m}$. In terms of DSMC cell units, 120 cells per linear direction are again sufficient to ensure a high accuracy for all the simulated cases. The Reynolds number is set to $Re = 0.1$. The agreement between DSMC simulations and the analytical expressions from Dahnek  is excellent, as presented in Fig. 5.

The cut-cell algorithm implemented and presented in this study has been incorporated in the parallel DSMC solver validated by Di Staso [54]. The intensive computations required for the DSMC simulations presented in this work, in fact, can become feasible only by taking advantage of parallel computation. This can be easily done for a DSMC algorithm, thanks to the locality of the interactions between gas molecules, by

enforcing a three-dimensional Cartesian processor grid on which the DSMC simulation domain is decomposed. The simulations presented in this work are executed on computational nodes with two AMD EPYC 7282 CPUs per node, and the individual run wall clock time strongly depends on the Knudsen number, ranging from 20 hours ($\text{Kn} \geq 10$) to several days ($\text{Kn} \sim 1$) on one node.

To conclude the characterization of the algorithm, an extensive convergence analysis of the mean value of the drag force experienced by the particle, and its standard deviation, is presented in Appendix B.

III. DRAG CORRELATIONS FOR ELLIPSOIDAL PARTICLES AT FINITE KNUDSEN NUMBER

In this section we investigate rarefaction and orientation effects on the drag force acting on prolate and oblate ellipsoidal particles, with the aim to provide the fundamental requirements for the predictive model presented in Sec. IV. Such requirements are embodied by the necessity first to define an expression for the Knudsen number for ellipsoidal particles that accurately (and consistently) captures rarefaction effects and, second to confirm the validity of the sine-squared drag law, introduced by Happel and Brenner [50] for the continuum regime, when rarefaction effects are present.

In relation to the definition of a single characteristic length for ellipsoidal particles, a number of authors [11,13,14,55] proposed to use the radius of the sphere with equivalent volume, R_{eq} , to define the Reynolds number. In this work we follow the same approach, extending this choice also to the Knudsen number, so that the relevant dimensionless numbers read $\text{Re} = 2U_0R_{eq}/\nu$, and $\text{Kn} = \lambda/R_{eq}$, where $\nu = \mu/\rho$ is the kinematic viscosity of the gas.

In this section, we show that the proposed definition of Kn is a good approximation to describe rarefaction effects for ellipsoidal particles. First, it successfully reduces the number of characteristic lengths to one (the radius of the equivalent sphere). This aspect not only defines Kn in an unambiguous way, but also makes this definition unrelated to the aspect ratio of the particle and to its orientation. Additionally, the relation between the drag force acting on the equivalent sphere and the one acting on the ellipsoidal particles is preserved independently of the specific value of Kn .

The necessity for rarefaction effects to be unrelated with a specific aspect ratio or orientation of the particle is a well-known result for the collisionless regime. A demonstration can be found in the analysis proposed by Bird [34], who expressed the drag and lift coefficients of a thin plate (i.e., a flat rectangular surface) immersed in a uniform gas flow as function of the molecular speed ratio, $s = U_0/(\frac{m}{2k_B T})^{1/2}$ [which represents the ratio between the ambient flow velocity, U_0 , and the most probable molecular speed $c_{mp} = (2k_B T/m)^{1/2}$], the angle of attack, Φ , and the temperature of the solid surface, T_{wall} . From these relations it can be shown that for small freestream velocities (i.e., $s \ll 1$) the correlation (represented by the sine-squared drag law) typical of the continuum limit is recovered, also for the collisionless case. It represents a clear indication that rarefaction effects are independent of the relative orientation between the particle and the incoming flow.

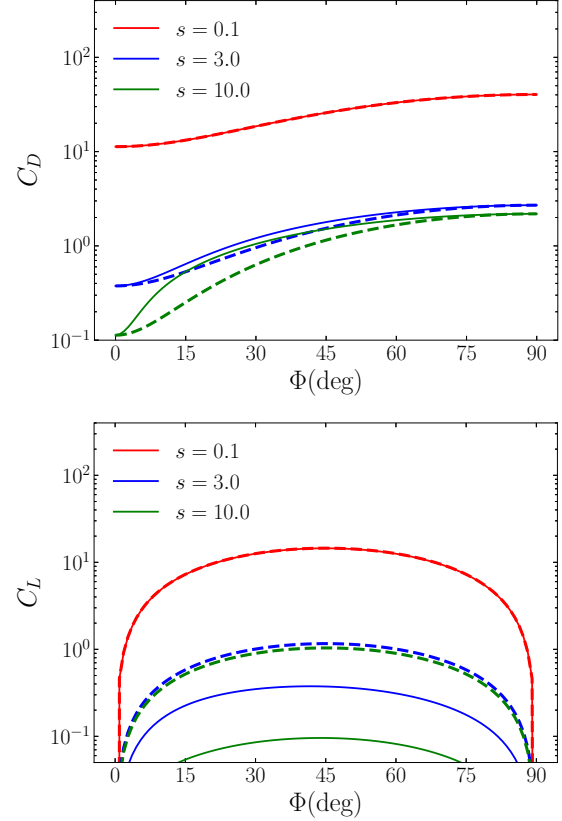


FIG. 6. Drag (top) and lift (bottom) coefficients (solid lines) as obtained by Bird [34] for a thin rectangular plate immersed in a collisionless gas flow for different speed ratios s , as a function of the angle of attack, Φ . The results are compared with the analytical correlations (dashed lines) from the continuum regime [50] given by Eqs. (9) and (10).

Using the linearity of velocity fields in creeping flows ($\text{Re} \ll 1$), Happel and Brenner [50] show that, in the continuum regime, the drag force on an arbitrary-shaped particle oriented at angle Φ with respect to the impinging flow can be expressed as

$$F_D(\Phi) = F_{D,0^\circ} + (F_{D,90^\circ} - F_{D,0^\circ}) \sin^2 \Phi, \quad (8)$$

where $F_{D,0^\circ}$ and $F_{D,90^\circ}$ are the drag forces at $\Phi = 0^\circ$ and $\Phi = 90^\circ$, respectively. It is useful to recall (see Fig. 1) that Eq. (8) is a general expression valid for any arbitrary orientation of the particle.

From Eq. (8), Happel and Brenner obtain the correlations for the drag and lift coefficients, which read

$$C_D(\Phi) = C_{D,0^\circ} + (C_{D,90^\circ} - C_{D,0^\circ}) \sin^2 \Phi, \quad (9)$$

$$C_L(\Phi) = (C_{D,90^\circ} - C_{D,0^\circ}) \sin \Phi \cos \Phi. \quad (10)$$

A confirmation of the validity of Eqs. (9) and (10) in the free-molecular regime is illustrated in Fig. 6, where we present the scaling of C_D and C_L for a thin rectangular plate, as proposed by Bird, as a function of the angle of attack, Φ , for different values of the speed ratio s . The results are then compared with respect to the correlations from the continuum regime given by Eqs. (9) and (10). It is shown that for small speed ratios the

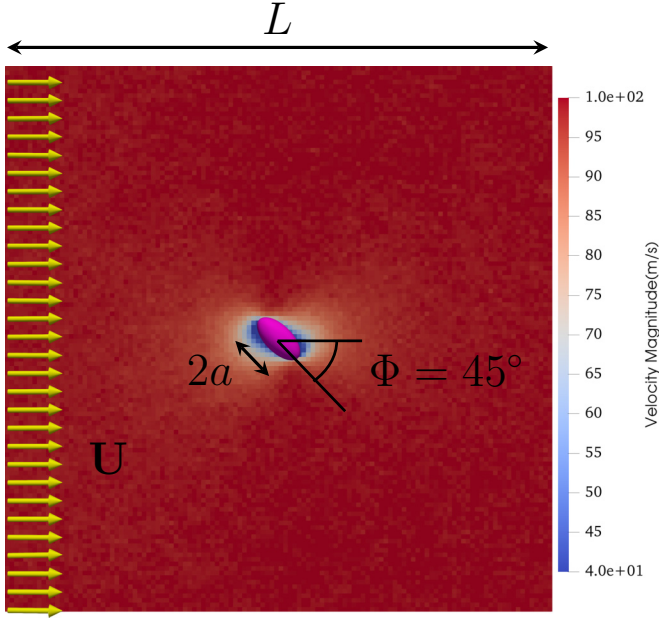


FIG. 7. Snapshot of the velocity field around a prolate ellipsoidal particle with aspect ratio $a/b = 2$ from a DSMC simulation. The plot represents a cut on the xy plane, crossing the particle center. The particle is immersed in an argon gas flow with freestream velocity \mathbf{U} (yellow arrows) and is oriented at $\Phi = 45^\circ$ with respect to the impinging gas flow. The simulation domain size is set such that $L \geq 20a$. In the case shown $\text{Kn} = 10$ and $\mathbf{U} = 99.7\hat{x}$ m/s.

correlations from the continuum regime indeed hold also in the collisionless limit, highlighting that rarefaction effects do not depend on the orientation of the solid body with respect to the gas flow. Since the sine-squared drag law is valid in both the continuum and the collisionless regimes, we expect it to be valid in the whole range of Knudsen numbers independently of the particle shape.

We verify this assumption by performing collisional DSMC simulations at varying $\text{Kn} = \lambda/R_{eq}$ and orientation Φ . Like in Sec. II B, the volume of the equivalent sphere is fixed to $V = 6.5 \times 10^{-20} \text{ m}^3$, corresponding to $R_{eq} = 2.5 \mu\text{m}$. The DSMC grid is set according to the requirements from [34,52], so that we use a value of $L = 140$ for $\text{Kn} = 1$ and a value of $L = 120$ for all other values of Kn ($2, \dots, 10$). A snapshot from the DSMC simulation for $\text{Kn} = 10$ and $\Phi = 45^\circ$ is presented in Fig. 7.

In Fig. 8, we compare the drag force on the ellipsoidal particles with the one acting on the equivalent sphere at the same Kn , as obtained by the prediction of Phillips from Eq. (6). The Φ dependence in Eq. (8) is well captured and rarefaction effects seem thus in good approximation independent of the orientation of the particle also for finite Kn , as the sine-squared drag law, obtained from the continuum regime, is preserved. Moreover, the relation between the drag force on the equivalent sphere and the one acting on the ellipsoidal particles is maintained for the investigated range of Kn , considering the presence of larger fluctuations at lower Kn cases due to lower kinetic resolution (i.e., the number of real particles described by a single computational particle). In all the investigated cases, in fact, $F_{\text{Phil}}(R_{eq})$ crosses the

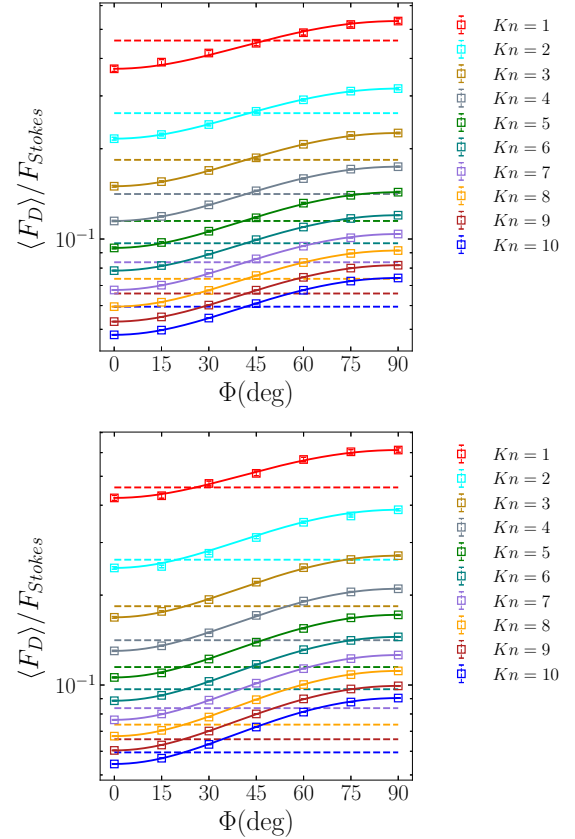


FIG. 8. Drag force from DSMC simulations for a prolate (top) and oblate (bottom) ellipsoid as a function of the Knudsen number Kn for different orientations Φ , normalized with respect to the Stokes drag of a spherical particle. The results from the DSMC simulations (squares) are compared with those for the sphere with equivalent volume (dashed lines) given by Eq. (6) and with the theoretical correlation (solid lines) obtained by inserting the values of $F_{D,0^\circ}$ and $F_{D,90^\circ}$ from our DSMC simulations into Eq. (8). The error bars are based on ε_{95} .

curves obtained from the simulations for the drag force on the ellipsoidal particle, and the intersection happens at $\Phi \sim 41^\circ$ and $\Phi \sim 22^\circ$ for the prolate and oblate cases, respectively.

The validity of the sine-squared drag law also in the presence of rarefaction is, *per se*, an important confirmation that can be used to build a predictive model for the drag force on ellipsoidal particles. While in this work we focus on simple uniform flows, it is interesting to investigate whether such a relation holds also in more complex situations, such as for particles with more complex shape, in the vicinity of solid walls or in cases where the Knudsen number varies across the fluid domain. We plan to address this class of problems in future studies.

IV. PREDICTIVE MODEL FOR THE DRAG AND LIFT COEFFICIENTS

In this section we propose the derivation of a heuristic model for the prediction of the drag and lift coefficients of prolate and oblate ellipsoidal particles. Such a model is based on the validity of the sine-squared drag law also in the presence

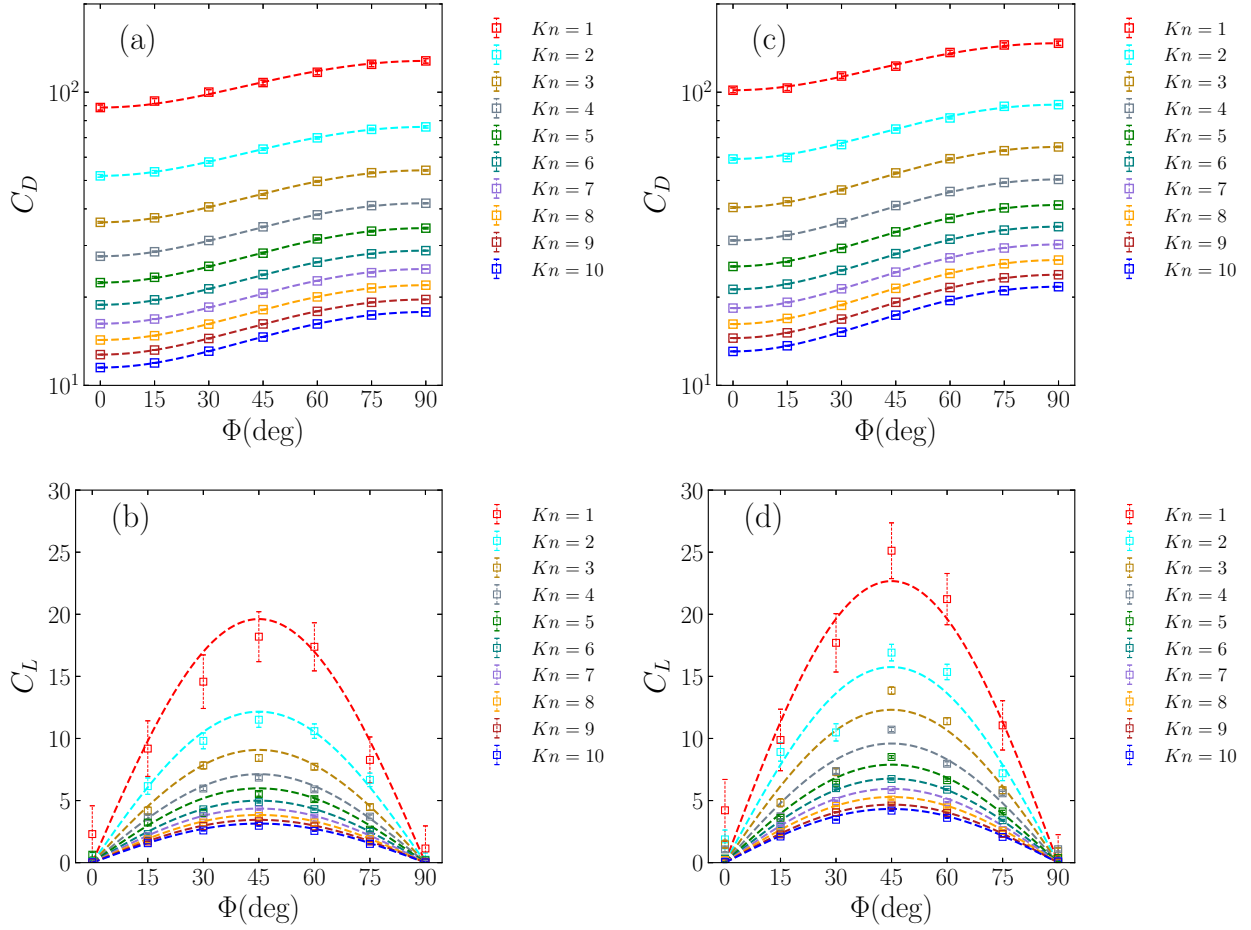


FIG. 9. Comparison between Eqs. (9) and (10) (dashed lines) and results from DSMC simulations (squares) for the drag (C_D) and lift (C_L) coefficients of (a, b) a prolate and (c, d) an oblate ellipsoid for different orientations Φ and Kn. Both ellipsoids have aspect ratio $a/b = 2$. In order to use Eqs. (9) and (10) in this context, we computed $C_{D,0^\circ}$ and $C_{D,90^\circ}$ directly from our DSMC simulations. The C_D data are plotted in semilog scale for a better readability.

of rarefaction and is aimed to extend the available correlations from the continuum to the rarefied regime. For our collisional DSMC simulations we maintain all the parameters the same as in Sec. III.

Following the work of Sanjeevi *et al.* [13], we define the drag and lift coefficients for an ellipsoidal particle as

$$C_D = \frac{|\mathbf{F}_D|}{\frac{1}{2}\rho U_0^2 \pi R_{eq}^2}, \quad (11)$$

$$C_L = \frac{|\mathbf{F}_L|}{\frac{1}{2}\rho U_0^2 \pi R_{eq}^2}, \quad (12)$$

where \mathbf{F}_L is the lift force acting on the particle, ρ is the density of the gas, U_0 is the gas freestream velocity. Since we are investigating uniform flows in the Stokes regime, the pitching torque is known to vanish in such conditions [56] due to the absence of an external rotational field, and thus the analysis of the pitching torque is not relevant in the scope of this work.

We can directly apply Eqs. (9) and (10) to obtain the analytical relations for the drag and lift coefficients, with respect to the angle of attack, Φ , of the simulated ellipsoidal particles. Here $C_{D,0^\circ}$ and $C_{D,90^\circ}$ can be obtained by measuring

the drag force experienced by the particles in our DSMC simulations and the results are shown in Fig. 9. As expected from the analysis presented in the previous section, simulation results are in excellent agreement with the theoretical predictions.

In the remainder of this section we will provide a heuristic model for $C_{D,0^\circ}$ and $C_{D,90^\circ}$ that takes into account rarefaction effects, in the attempt to include in Eqs. (9) and (10) a dependence on the Knudsen number. Our starting assumption is that, similarly to the spherical case, an equation for C_D that includes rarefaction effects for ellipsoidal particles can be written as a product between C_D in the continuum limit and a function $g(\text{Kn})$ which represents a small perturbation with respect to the spherical case:

$$C_{D,0^\circ}(\text{Kn}) = \underbrace{C_{D,0^\circ}^{\text{cont}}}_{\text{continuum}} \times \underbrace{g_{0^\circ}(\text{Kn})}_{\text{rarefaction effects}}, \quad (13)$$

$$C_{D,90^\circ}(\text{Kn}) = \underbrace{C_{D,90^\circ}^{\text{cont}}}_{\text{continuum}} \times \underbrace{g_{90^\circ}(\text{Kn})}_{\text{rarefaction effects}}, \quad (14)$$

where $C_{D,0^\circ}^{\text{cont}}$ and $C_{D,90^\circ}^{\text{cont}}$ are the drag coefficients in the continuum regime, while $g_{0^\circ}(\text{Kn})$ and $g_{90^\circ}(\text{Kn})$ are model functions to be evaluated. In order to use Eqs. (13) and (14), we first

TABLE I. Values of $C_{D,0^\circ}$ and $C_{D,90^\circ}$ (three-digit accuracy) for prolate and oblate ellipsoids with aspect ratio $a/b = 2$. Results are obtained from the theoretical prediction given by Eqs. (16) and (17) using the correction factors from Eqs. (18)–(21) and the expression for C_D^{sph} from Eq. (15).

	Prolate	Oblate
$C_{D,0^\circ}$	236	247
$C_{D,90^\circ}$	270	282

need to compute the values of $C_{D,0^\circ}^{\text{cont}}$ and $C_{D,90^\circ}^{\text{cont}}$ for the ellipsoidal particles investigated in this work. This can be done using the Schiller-Neumann [57] drag expression for the drag coefficient of a spherical particle,

$$C_D^{sph} = \frac{24}{\text{Re}}(1 + 0.15\text{Re}^{0.687}), \quad (15)$$

which has proven to be quite accurate up to a moderate Reynolds number. We can then obtain $C_{D,0^\circ}^{\text{cont}}$ and $C_{D,90^\circ}^{\text{cont}}$ for the simulated ellipsoidal particles using the heuristic relations from Happel and Brenner [50]:

$$C_{D,0^\circ}^{\text{cont}} = C_D^{sph} K_{0^\circ}, \quad (16)$$

$$C_{D,90^\circ}^{\text{cont}} = C_D^{sph} K_{90^\circ}. \quad (17)$$

The correction factors K_{0° and K_{90° depend on the shape of the particle and, for regular prolate and oblate ellipsoidal particles in creeping flow conditions, the exact analytical expressions for the correction factors were derived by Oberbeck [4] as a function of their major and minor axes a and b , respectively:

$$K_{0^\circ}^{pr} = \frac{(4/3)(a/b)^{-1/3}(1 - (a/b)^2)}{a/b - \frac{(2(a/b)^2 - 1) \ln((a/b) + \sqrt{(a/b)^2 - 1})}{\sqrt{(a/b)^2 - 1}}}, \quad (18)$$

$$K_{90^\circ}^{pr} = \frac{(8/3)(a/b)^{-1/3}((a/b)^2 - 1)}{a/b + \frac{(2(a/b)^2 - 3) \ln((a/b) + \sqrt{(a/b)^2 - 1})}{\sqrt{(a/b)^2 - 1}}}, \quad (19)$$

$$K_{0^\circ}^{ob} = \frac{(8/3)(b/a)^{-1/3}((b/a)^2 - 1)}{b/a - \frac{(3 - 2(b/a)^2) \cos^{-1}(b/a)}{\sqrt{1 - (b/a)^2}}}, \quad (20)$$

$$K_{90^\circ}^{ob} = \frac{(4/3)(b/a)^{-1/3}(1 - (b/a)^2)}{b/a + \frac{(1 - 2(b/a)^2) \cos^{-1}(b/a)}{\sqrt{1 - (b/a)^2}}}. \quad (21)$$

Ouchene *et al.* [11] showed that for creeping flows, the set of Eqs. (18)–(21) predicts the drag coefficients of prolate ellipsoids with different aspect ratios with very high accuracy. We then compute $C_{D,0^\circ}^{\text{cont}}$ and $C_{D,90^\circ}^{\text{cont}}$ by substituting Eq. (15) into Eqs. (16) and (17), using the corrections given by Eqs. (18)–(21). The results are shown in Table I, and can be used in Eqs. (16) and (17) to obtain C_D for the ellipsoidal particles used in this work.

To address rarefaction effects, we propose the following choice for the general expression of the functions $g_{0^\circ}(\text{Kn})$ and $g_{90^\circ}(\text{Kn})$, where we assume that such effects on ellipsoidal

particles can be described as small variations with respect to the function $f(\text{Kn})$ for the spherical case:

$$g_{0^\circ}(\text{Kn}) = f(\text{Kn}) + \frac{a_{0^\circ}}{b_{0^\circ} + c_{0^\circ} \text{Kn}}, \quad (22)$$

$$g_{90^\circ}(\text{Kn}) = f(\text{Kn}) + \frac{a_{90^\circ}}{b_{90^\circ} + c_{90^\circ} \text{Kn}}, \quad (23)$$

where a , b , and c are free parameters to be determined separately for $C_{D,0^\circ}$ and $C_{D,90^\circ}$.

We show that with the proposed choice of the $g(\text{Kn})$ functions, it is sufficient to fit the model on a small set of Kn to obtain a robust predictive model for rarefaction effects on ellipsoidal particles. The simulation data are split into two groups:

$$\text{Kn}_{\text{fit}} = 2, 5, 8, 10,$$

$$\text{Kn}_{\text{test}} = 1, 3, 4, 6, 7, 9, 20.$$

We then perform a fit of $C_{D,0^\circ}$ and $C_{D,90^\circ}$ from simulation data as a function of Kn , using only the Kn_{fit} set and the fit functions given by Eqs. (13) and (14). The results of the fit are shown in Fig. 10 and the obtained fit parameters are given in Table II. Now Eqs. (22) and (23) are fully defined and we can proceed with the test of the model.

Once the functions $g(\text{Kn})$ are determined for the needed orientations, we can verify if the model succeeds in the

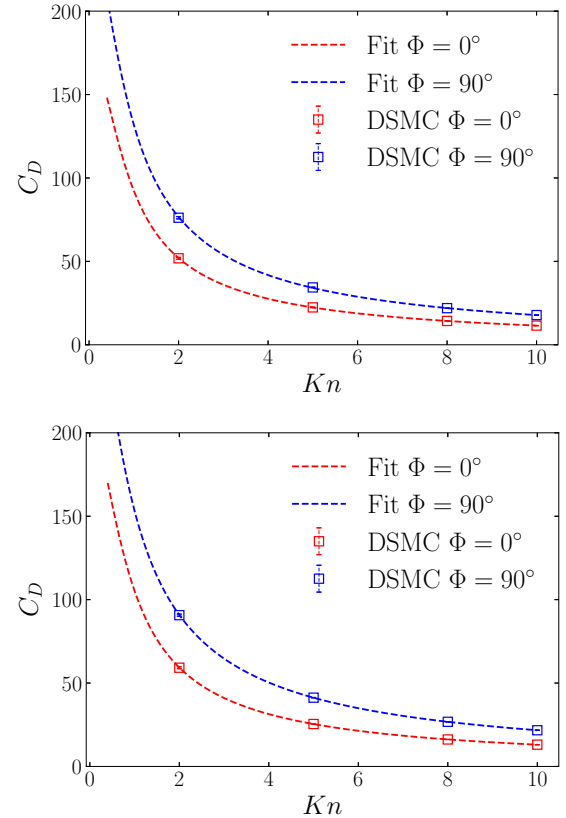


FIG. 10. Fit of DSMC simulation data of $C_{D,0^\circ}$ (red) and $C_{D,90^\circ}$ (blue) using the functions in Eqs. (22) and (23), for a prolate ellipsoid (top) and an oblate ellipsoid (bottom). Fitted curves (dashed lines) represent the model functions given by Eqs. (13) and (14). The resulting fit parameters are presented in Table II.

TABLE II. Fit parameters obtained using Eqs. (13) and (14) to fit $C_{D,0^\circ}$ and $C_{D,90^\circ}$ as obtained from DSMC simulations. These parameters are used to define the functions $g_{0^\circ}(\text{Kn})$ and $g_{90^\circ}(\text{Kn})$, for which a general expression is given in Eqs. (22) and (23).

	Prolate		Oblate	
	$\Phi = 0^\circ$	$\Phi = 90^\circ$	$\Phi = 0^\circ$	$\Phi = 90^\circ$
a	-0.171	0.115	-0.219	0.223
b	1.023	2.492	3.762	1.523
c	1.482	1.603	2.916	1.126

prediction of C_D at different values of Kn and Φ . In order to do so we plug Eqs. (13) and (14) into Eq. (9) to obtain the final model equation for $C_D(\Phi, \text{Kn})$:

$$C_D(\Phi, \text{Kn}) = C_{D,0^\circ}^{\text{cont}} g_{0^\circ}(\text{Kn}) + (C_{D,90^\circ}^{\text{cont}} g_{90^\circ}(\text{Kn}) - C_{D,0^\circ}^{\text{cont}} g_{0^\circ}(\text{Kn})) \sin^2 \Phi. \quad (24)$$

The comparison between Eq. (24) and the results from DSMC simulation is performed on both the data sets Kn_{fit} and Kn_{test} , where the latter set has not been used during the fit process. The results are shown in Fig. 11, where we can observe an excellent agreement between the proposed model and the simulations. Particularly relevant is the agreement between the model and the data for Kn_{test} , showing that the model correctly predicts rarefaction effects on values of Kn that were

not included in the fitting process and it can be extended to the regimes with $\text{Kn} \leq 2$ and $\text{Kn} \geq 10$.

In an analogous way, we investigate the capability of the predictive model given by Eqs. (13) and (14) to address the lift coefficient C_L of the different ellipsoids. Following the same approach we used for the evaluation of C_D , we plug Eqs. (13) and (14) into Eq. (10) to obtain the model equation for C_L :

$$C_L(\Phi, \text{Kn}) = (C_{D,90^\circ}^{\text{cont}} g_{90^\circ}(\text{Kn}) - C_{D,0^\circ}^{\text{cont}} g_{0^\circ}(\text{Kn})) \sin \Phi \cos \Phi. \quad (25)$$

We can now compare the prediction from Eq. (25) with the C_L obtained from the DSMC simulations, again using the same approach to separate the data into Kn_{fit} and Kn_{test} . The results of the comparison are shown in Fig. 12. The model prediction is in reasonable agreement with the simulation data, considering that $C_L \ll C_D$, leading to a lower signal-to-noise ratio from the DSMC simulations for C_L with respect to C_D .

In the last part of this paper, we compare the performances of the predictive model proposed in this work with existing phenomenological models available in the literature used to predict the drag on nonspherical particles at different Knudsen numbers, namely, the previously mentioned ESA and ASA, as defined by Dahneke [33]. The former consists in the direct application of the Cunningham corrections [20] on the sphere with equivalent volume of the investigated particle, so that any information on the orientation is lost and this model offers a

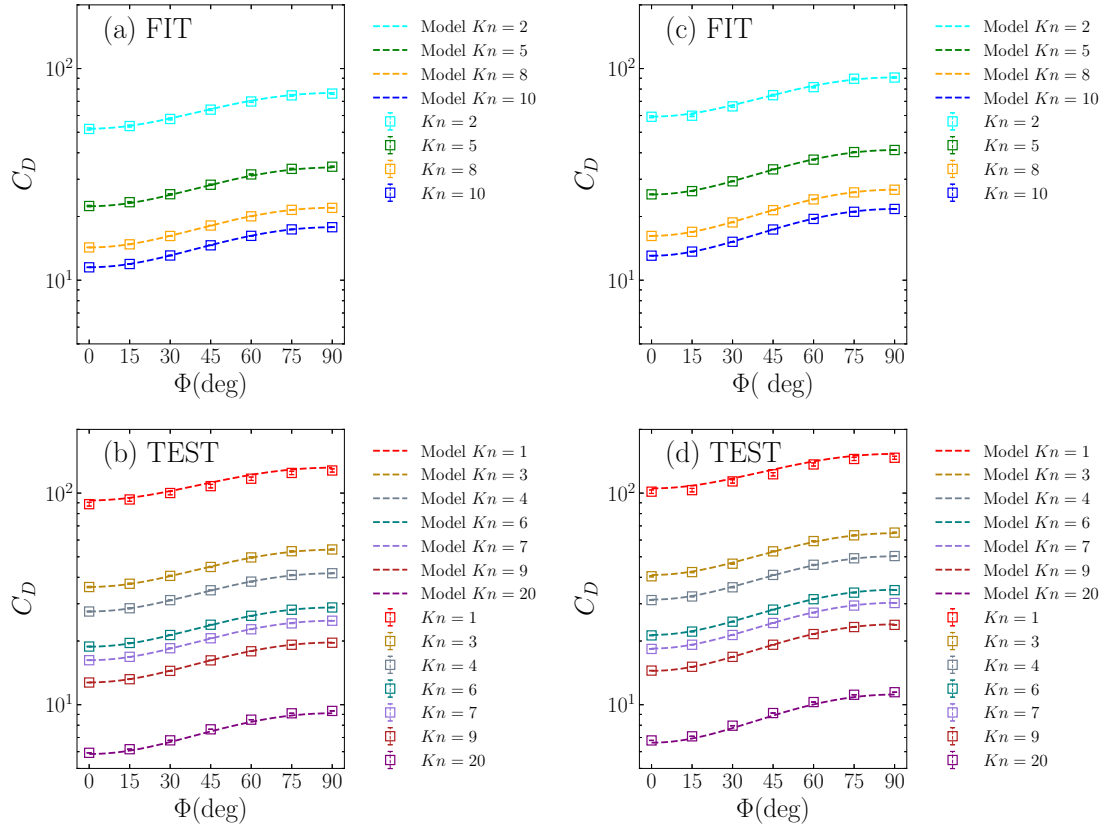


FIG. 11. Comparison between DSMC simulations (colored squares) and model predictions (colored dashed lines) of the drag coefficient C_D of (a, b) a prolate and (c, d) an oblate ellipsoid. The model predictions, given by Eq. (24), are then compared with (a, c) the fit set and (b, d) the test set. In both cases the match is excellent.

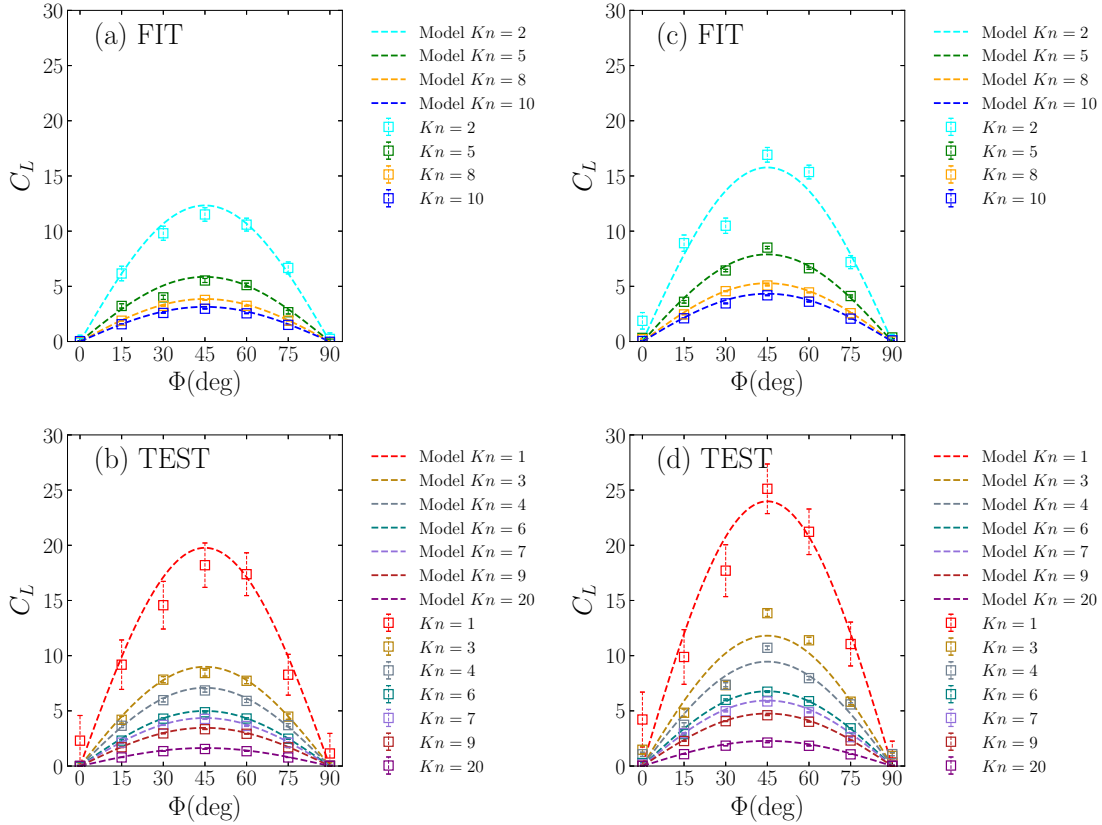


FIG. 12. Comparison between the lift coefficient C_L from DSMC simulations (colored squares) and the predictive model (dashed lines) for (a, b) a prolate and (c, d) an oblate ellipsoid. The model predictions, given by Eq. (25) are then compared with (a, c) the fit set and (b, d) the test set.

good accuracy only for slightly nonspherical bodies. The latter is a more sophisticated model where spheres with different effective radii are used to match the rarefaction corrections experienced by the particle under investigation at specific orientations. Such corrections must have been previously determined by evaluating the ratio between the continuum and free molecular drag force acting on the particle.

The results of the comparison, limited to some of the values in the Kn_{test} set, are presented in Fig. 13, where we use the results provided by [33] to compute the ASA prediction for the spheroidal particles investigated in this work. The performances of the proposed model in reproducing C_D show a general improvement with respect to the ASA model, and this is particularly evident for the oblate case. This is due to the larger departure from the spherical case of oblate ellipsoids, as the ASA model appears to be less accurate the higher this departure is.

The presented approach is proven to be successful in predicting rarefaction effects on the forces exerted on ellipsoidal particles, and shows that it is possible to describe such effects with a perturbative approach from the spherical case. Our results are, however, currently limited to the investigated aspect ratio ($a/b = 2$) and for fully diffusive surfaces ($\sigma = 1$). In our future works we plan to extend the predictive model to a larger range of aspect ratios, including also effects from a momentum accommodation coefficient σ lower than unity to take into account the presence of specular reflections to model more realistic gas-surface interactions.

V. CONCLUSIONS

In conclusion, we developed a two-way coupled algorithm to address interactions, under rarefied conditions, between gas flows and spheroidal particles based on momentum exchange for our in-house DSMC numerical code. The surface of the solid particle is defined by its analytical expression and the interactions between the gas and the rigid body are computed from a microscopic approach. The collision points at which the computational molecules impinge on the solid surface are obtained through a ray-tracing technique, allowing an exact computation of the collision points of the gas molecules impinging on the solid surface.

The algorithm features the cut-cell method to address the DSMC grid cells that are partially covered by the solid volume. We use a Monte Carlo approach to evaluate the volume of the boundary cells, showing that for an appropriate number of trials, it is possible to recover the volume of the interested cells with great accuracy.

The algorithm is validated by computing the drag force on spherical and ellipsoidal particles immersed in a uniform argon gas flow in different conditions. We show that the measurements from our simulations are in good agreement with different results available in the literature, especially when compared with analogous DSMC methods. The accuracy scaling of the mean value and of the standard deviation of the drag force is investigated with respect to the spatial and kinetic resolutions of the system in Appendix B.

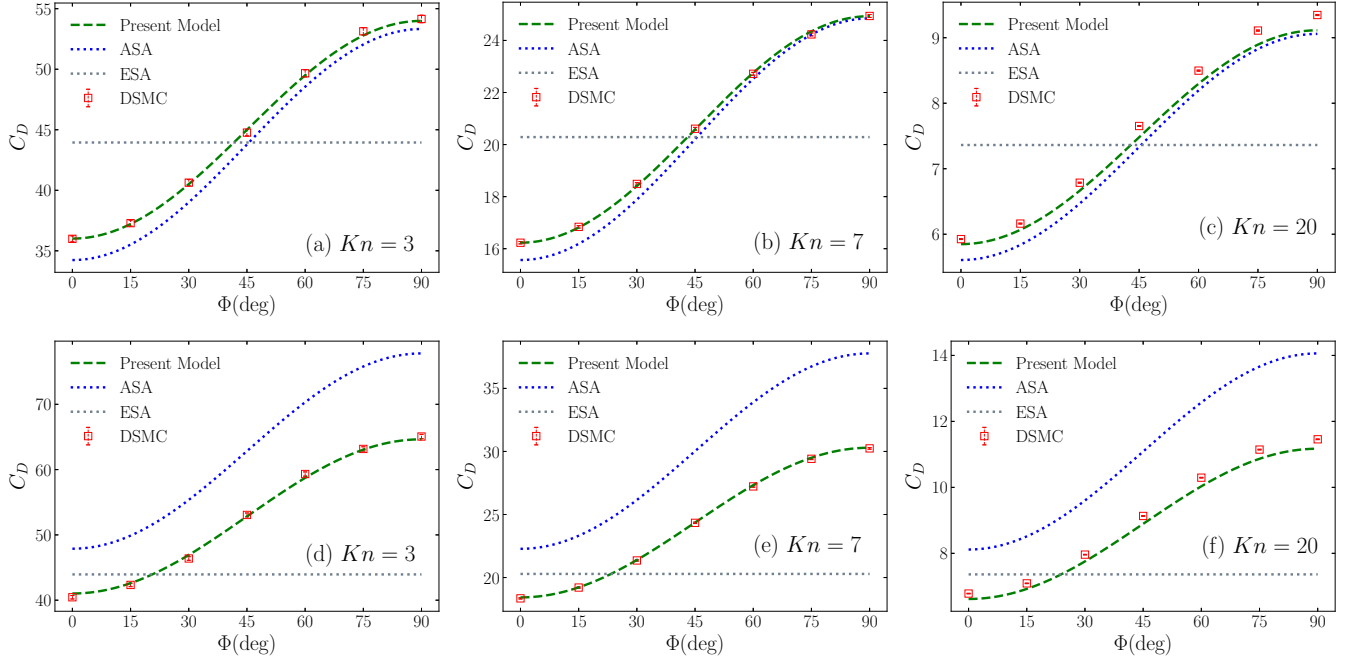


FIG. 13. Comparison of the C_D predictions as obtained with the present model (green dashed line), and with the ASA (blue dotted line) and ESA (gray dotted line) models as defined in [33] for different values of Kn from the Kn_{test} for (a–c) a prolate and (d–f) an oblate ellipsoid with internal aspect ratio $a/b = 2$. The predictions from the models are also compared with direct results from DSMC simulations (red squares).

We then address the impact of shape, orientation, and rarefaction on the drag force for a prolate and an oblate ellipsoid. We first propose a suitable definition of the Knudsen number, Kn , for ellipsoidal particles based on the radius of the sphere of equivalent volume and then we show that the sine-squared drag law typical of the continuum regime is valid also in the presence of rarefaction. Orientation and rarefaction effects are, in fact, not related, and it is possible to address them separately.

Finally, we develop a heuristic model to predict the drag and lift coefficients for ellipsoidal particles in a range of Kn that includes the transition and the free-molecular regimes. The predictive model is based on the assumption that rarefaction effects on ellipsoidal particles can be represented as small perturbations with respect to the spherical case. These perturbations are obtained through a fit of our simulation data. The model obtained with this procedure shows robust performance in predicting drag and lift coefficients in the investigated range of Kn , and we show that the model can be successfully applied outside of the range of Kn used for its derivation. Moreover, the model proposed in this work offers better predictions when compared to phenomenological models such as the ESA and the ASA, especially for the oblate ellipsoid case, where the shape of the particle largely deviates from the spherical case.

We emphasize that the results from this work can be used to improve the available models used in Euler-Lagrangian simulations of particles in rarefied conditions, as the drag and lift correlations can now be extended to the rarefied regimes. This allows in principle to include shape and orientation effects in point-particles simulations, greatly increasing the capability to simulate suspensions of nonspherical particles in rarefied gas flows, which are expected to follow different trajectories with respect to the spherical case. Such a feature is of valuable

interest in modern high-tech applications, as it can help to improve the state-of-the-art techniques typically employed to address problems such as contamination from particles in low-pressure environments.

While we show results for particles with aspect ratio $a/b = 2$ and with fully diffusive surface, in our future works we plan to extend the proposed technique to ellipsoids with different complex aspect ratios, such as needles and disks, and to include a study of the impact of different momentum accommodation coefficients, by taking into account the presence of specular reflections at the gas-solid interface.

ACKNOWLEDGMENTS

This work was supported by the Netherlands Organization for Scientific Research (NWO-TTW), under Project No. 15376.

APPENDIX A: DETAILS OF THE GAS-SURFACE INTERACTION ALGORITHM

In this Appendix the details of the algorithm used in this work for the detection of the collision points between the DSMC molecules and surface of a solid generic ellipsoidal object are further described.

Two Cartesian coordinate systems are employed: the inertial frame, (x, y, z) , attached to the computational domain, and the body-centered frame, (x', y', z') , which is instead attached to the center of mass of the particle and is aligned along the principal direction of inertia of the particle. To transform the inertial frame into the body-centered frame, first we perform a negative translation of $\mathbf{X} = (X, Y, Z)$, representing the coordinates of the center of mass of the particle.

A sketch of the collision detection algorithm is shown in Fig. 14.

$$M = \begin{pmatrix} q_0^2 + q_1^2 - q_2^2 - q_3^2 & 2(q_1q_2 + q_0q_3) & 2(q_1q_3 - q_0q_2) \\ 2(q_1q_2 - q_0q_3) & q_0^2 - q_1^2 + q_2^2 - q_3^2 & 2(q_2q_3 + q_0q_1) \\ 2(q_1q_3 + q_0q_2) & 2(q_2q_3 - q_0q_1) & q_0^2 - q_1^2 - q_2^2 + q_3^2 \end{pmatrix}, \quad (\text{A1})$$

where we use the four quaternion variables,

$$q_0 = \cos(\theta/2) \cos((\Phi + \Psi)/2), \quad (\text{A2})$$

$$q_1 = \sin(\theta/2) \cos((\Phi - \Psi)/2), \quad (\text{A3})$$

$$q_2 = \sin(\theta/2) \sin((\Phi - \Psi)/2), \quad (\text{A4})$$

$$q_3 = \cos(\theta/2) \sin((\Phi + \Psi)/2), \quad (\text{A5})$$

defined from the Euler angles (θ, Φ, Ψ) sketched in Fig. 15. A final transformation is then enforced to ensure that in the final reference system (x', y', z') any generic ellipsoidal particle is described as a spherical particle with unitary radius. Such stretch along the main axes is represented by the matrix S :

$$S = \begin{pmatrix} 1/a & 0 & 0 \\ 0 & 1/b & 0 \\ 0 & 0 & 1/c \end{pmatrix}, \quad (\text{A6})$$

where a , b , and c are the radii of the ellipsoidal particle. The final transformation equation for a generic point \mathbf{x} in the inertial reference frame into its equivalent \mathbf{x}' in the stretched body-centered frame thus reads

$$\mathbf{x}' = SM(\mathbf{x} - \mathbf{X}). \quad (\text{A7})$$

In the framework of the DSMC method, we apply Eq. (A7) to transform the pre- and poststreaming positions \mathbf{x}_0 and \mathbf{x}_f of the

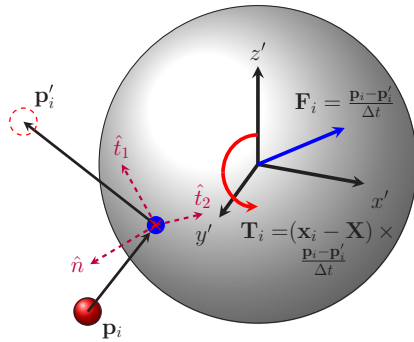


FIG. 14. Sketch of the gas-solid interaction scheme. An impinging gas molecule i (red sphere) with initial momentum \mathbf{p}_i hits the surface of the solid particle (gray sphere) and undergoes a diffusive reflection with postcollisional momentum \mathbf{p}'_i , where the collision point (red cross) is evaluated exactly in the body-centered reference system (x', y', z') . Then, the reflections are computed in the reference system formed by the normal and tangent unit vectors, $(\hat{n}, \hat{t}_1, \hat{t}_2)$, with respect to the surface of the particle. Finally, the postcollisional position and velocity are transformed back in the inertial reference system.

The translation is followed by a rotation defined by the matrix M :

impinging DSMC molecules in the body-centered stretched reference system:

$$\mathbf{x}'_0 = SM(\mathbf{x}_0 - \mathbf{X}), \quad (\text{A8})$$

$$\mathbf{x}'_f = SM(\mathbf{x}_f - \mathbf{X}). \quad (\text{A9})$$

Then, the ray-sphere intersection algorithm simply consists in the evaluation of the intersections between the unit radius sphere centered in the origin (which represent the transformed particle) and the parametric line, $L(t)$, passing from \mathbf{x}'_0 and \mathbf{x}'_f with unitary direction \mathbf{v}' , given by

$$L(t) = \mathbf{x}'_0 + t\mathbf{v}'. \quad (\text{A10})$$

The intersection points are found by substituting the generic point on the sphere with a generic point on the line $L(t)$ and resolving for the free parameter t . The final quadratic equation reads

$$(\mathbf{v}' \cdot \mathbf{v}')t^2 + 2(\mathbf{v}' \cdot \mathbf{x}'_0)t + (\mathbf{x}'_0 \cdot \mathbf{x}'_0) = 1, \quad (\text{A11})$$

whose solutions, t_1 and t_2 , allow to calculate the intersection points by inserting them into Eq. (A10). To ensure the selection of the correct collision points, only the values of t_1 and t_2 that satisfy the condition $\|L(t) - \mathbf{x}'_0\| \leq \|\mathbf{x}'_f - \mathbf{x}'_0\|$ are considered. If both points respect this condition, then the point closer to \mathbf{x}'_0 is chosen. The reflection scheme is then applied in the reference system formed by the normal and tangent unit vectors, with respect to the surface of the particle, with origin in the collision point and given by $(\hat{n}, \hat{t}_1, \hat{t}_2)$. In this way the collision routine is equivalent as the one employed for a planar wall reported for example in [52]. The final position and velocities after reflection are then transformed back in the inertial reference frame.

It is possible to extend the algorithm to particles with different shapes by employing a different ray-surface intersection algorithm and its relative coordinates transformation. Some examples of such intersection algorithms for the most common shapes, such as boxes, cones, and triangles, can be found in [51]. Ultimately, a particle with a complex shape can be described by an opportune combination of these known shapes, and intersections can be found using the appropriate ray-surface intersection scheme for each one of the constituent basic shapes, separately. In the more general case, a triangulation of the surface can be applied and then a ray-triangle intersection scheme can be used.

APPENDIX B: ACCURACY SCALING OF THE CUT-CELL ALGORITHM

In this Appendix, we aim to investigate the accuracy scaling of the cut-cell algorithm proposed in this work with

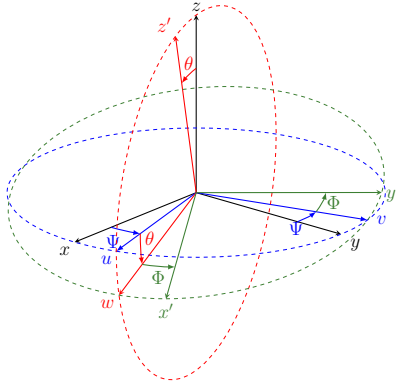


FIG. 15. Euler angles representation. Any rotation of the coordinate system (x, y, z) (black) can be described by a precession rotation around the axis z by an angle Ψ , which leads to the auxiliary system (u, v, z) (blue), followed by a nutation rotation of an angle θ around the axis v to obtain the second auxiliary system (w, u, z') (red), and finally by a rotation of Φ around z' to obtain the reference system (x', y', z') (green).

respect to spatial and kinetic resolution, separately. The former is related to the impact of different sizes of the particles (in cell units) and is embodied by the parameters L_c/λ and the particle radius R . The latter represents the number of real particles described by a computational particle and is tuned

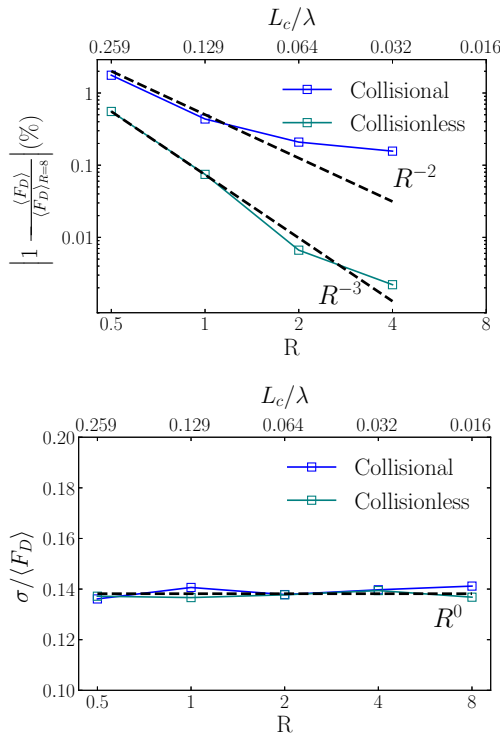


FIG. 16. Relative error (top) and standard deviation (bottom) of the mean value of the drag force, $\langle F_D \rangle$, for a spherical particle at $\text{Kn} = 10$, as a function of the spatial resolution of the solid particle R . Results from collisional (blue) and collisionless (green) DSMC simulations are included. The relative error is computed with respect to the value of $\langle F_D \rangle$ measured at $R = 8$.

via the number of particles per cell, N_c . This kind of analysis is, to our knowledge, not available in the literature, and it is important to understand the impact of different parameters, such as the resolution of the solid particle and the number of particles per cell, on the accuracy of the DSMC simulations.

In the first analysis, we compare the relative error on the mean value and the standard deviation of the drag force on a spherical particle at $\text{Kn} = 10$ for different values of the particle radius, R (in cells units). This is done by fixing the total number of DSMC molecules and by fixing the simulation time step, to ensure that the number of collisions per time step is unchanged between different resolutions. We do so to isolate the effects induced by varying the simulation grid size on the overall simulation accuracy. The ratio between the simulation box size and the particle radius is fixed to $L/R = 20$, so that varying the resolution of the particles is equivalent to varying the value of the DSMC spatial resolution given by L_c/λ . By imposing the same time step between different simulations we finally ensure that the number of collisions per time step between the DSMC molecules and the solid particle is the same for all the simulations, leading to a constant standard deviation.

The results are shown in Fig. 16, where we observe that when intermolecular collisions are present, the relative error on the mean value of the drag force exhibits a second-order scaling with respect to the spatial resolution for small

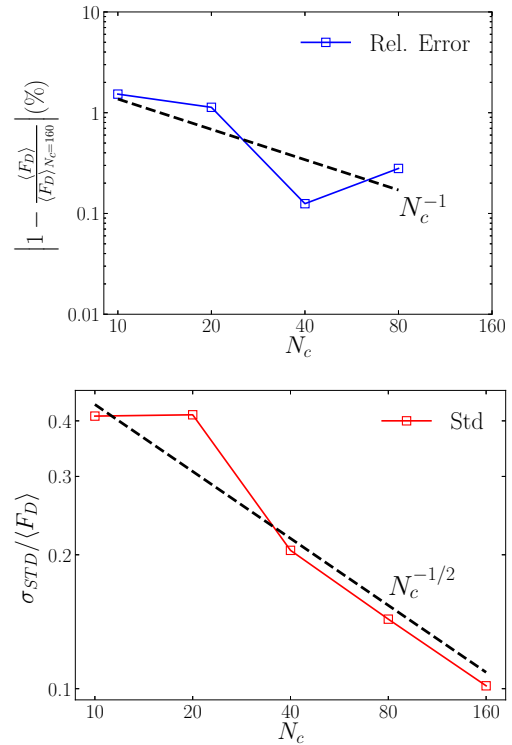


FIG. 17. Relative error (top) and standard deviation (bottom) of the mean value of the drag force, $\langle F_D \rangle$, for a spherical particle at $\text{Kn} = 10$, as a function of the kinetic resolution, given by the number of particles per cell, N_c . In this analysis the ratio between the simulation box size and the radius of the particle is $L/R = 20$ and the radius of the particle is set to $R = 4$. The relative error is computed with respect to the value of $\langle F_D \rangle$ measured at $N_c = 160$.

values of R , while it deviates from the scaling law for larger values of R . This deviation is related to the approaching of the DSMC resolution limits in resolving stochastic intermolecular collisions as, in this setup, the number of particles per cell, N_c , decreases for increasing R as a consequence of keeping the total number of particles unchanged. Once intermolecular collisions are switched off, in fact, the error is drastically reduced and it shows a consistent third-order convergence with respect to spatial resolution. Interestingly, the algorithm offers a remarkable good accuracy also for cases where the radius of the particle is of the order of one

DSMC cell, allowing to correctly resolve the drag for particles with a small curvature with respect to the DSMC spatial grid resolution.

We checked also the accuracy scaling with respect to the kinetic resolution. This is done by fixing the particle radius to $R = 4$ (and thus $L_c/\lambda = 0.032$) and by varying the number of particles per cell, N_c . Results are shown in Fig. 17, where it can be observed that the scaling of both the mean value of the drag force and of its standard deviation are in agreement with the typical results of a DSMC simulation, with the former scaling linearly with N_c and the latter scaling as $N_c^{-1/2}$.

-
- [1] C. Wang, S. K. Friedlander, and L. Mädler, *China Particuol.* **3**, 243 (2005).
- [2] A. K. Bates, M. Rothschild, T. M. Bloomstein, T. H. Fedynyshyn, R. R. Kunz, V. Liberman, and M. Switkes, *IBM J. Res. Dev.* **45**, 605 (2001).
- [3] C. Kleinstreuer and Y. Feng, *J. Biomech. Eng.* **135**, 021008 (2013).
- [4] A. Oberbeck, *J. Reine Angew. Math. (Crelle's J.)* **81**, 62 (1876).
- [5] G. B. Jeffery, *P. Roy. Soc. A-Math. Phys.* **102**, 715 (1922).
- [6] A. Haider and O. Levenspiel, *Powder Technol.* **58**, 63 (1989).
- [7] G. H. Ganser, *Powder Technol.* **77**, 143 (1993).
- [8] A. Hölzer and M. Sommerfeld, *Comput. Fluids* **3**, 572 (2009).
- [9] M. Zastawny, G. Mallouppas, F. Zhao, and B. Van Wachem, *Int. J. Multiphase Flow* **39**, 227 (2012).
- [10] P. A. Nikrityuk and A. Richter, *Powder Technol.* **249**, 463 (2013).
- [11] R. Ouchene, A. Taniere, and B. Arcen, *Comput. Fluids* **13**, 53 (2015).
- [12] C. Livi, G. Di Staso, H. J. H. Clercx, and F. Toschi, *Phys. Rev. E* **103**, 013303 (2021).
- [13] S. K. P. Sanjeevi and J. T. Padding, *J. Fluid Mech.* **820**, R1 (2017).
- [14] S. K. P. Sanjeevi, J. A. M. Kuipers, and J. T. Padding, *Int. J. Multiphase Flow* **106**, 325 (2018).
- [15] X. Xheng and Z. Silber-Li, *Appl. Phys. Lett.* **95**, 124105 (2009).
- [16] X. Shen and D. B. Bogy, *J. Tribol.* **125**, 358 (2003).
- [17] S. Zhang and D. B. Bogy, *Phys. Fluids* **9**, 1265 (1997).
- [18] O. Abouali, A. Nikbakht, G. Ahmadi, and S. Saadabadi, *Aerosol Sci. Technol.* **43**, 205 (2009).
- [19] K. Zhang, H.-B. Xiong, and Z.-M. Shao, *J. Zhejiang Univ.-Sci. A* **17**, 733 (2016).
- [20] E. Cunningham, *Proc. R. Soc. Lond. A* **83**, 357 (1910).
- [21] V. C. Liu, S. C. Pang, and H. Jew, *Phys. Fluids* **8**, 788 (1965).
- [22] P. S. Epstein, *Phys. Rev.* **23**, 710 (1924).
- [23] M. J. Baines, I. P. Williams, A. S. Asebiomo, and R. L. Agacy, *Mon. Not. R. Astron. Soc.* **130**, 63 (1965).
- [24] M. A. Gallis, J. R. Torczynski, and D. J. Rader, *Phys. Fluids* **13**, 3482 (2001).
- [25] M. A. Gallis, D. J. Rader, and J. R. Torczynski, *Aerosol Sci. Technol.* **36**, 1099 (2002).
- [26] W. F. Phillips, *Phys. Fluids* **18**, 1089 (1975).
- [27] L. Lees, *J. Soc. Ind. Appl. Math.* **13**, 278 (1965).
- [28] L. Lees and C. Y. Liu, *Phys. Fluids* **5**, 1137 (1962).
- [29] R. A. Millikan, *Phys. Rev.* **32**, 349 (1911).
- [30] R. A. Millikan, *Phys. Rev.* **22**, 1 (1923).
- [31] J. Halbritter, *Z. Naturforsch.* **29a**, 1717 (1974).
- [32] B. E. Dahnekë, *J. Aerosol Sci.* **4**, 147 (1972).
- [33] B. E. Dahnekë, *J. Aerosol Sci.* **4**, 163 (1972).
- [34] G. A. Bird, *Molecular Gas Dynamics and the Direct Simulation of Gas Flows* (Clarendon, Oxford, 1994).
- [35] S. K. Stefanov, *Phys. Fluids* **31**, 067104 (2019).
- [36] G. Karniadakis, A. Beskok, and N. Aluru, *Microflows and Nanoflows: Fundamentals and Simulation* (Springer-Verlag, New York, 2005).
- [37] M. Reese, M. A. Gallis, and D. A. Lockerby, *Philos. Trans. R. Soc. London A* **361**, 2967 (2003).
- [38] R. Wilmoth, A. Carlson, and G. LeBeau, in *Proceedings of the 31st Thermophysics Conference 17-20 June 1996 New Orleans, LA* (AIAA, Reston, VA, 1996), AIAA Paper 96-1812.
- [39] G. J. LeBeau, *Comput. Methods Appl. Mech. Eng.* **174**, 319 (1999).
- [40] C. Zhang and T. E. Schwartzentruber, *Comput. Fluids* **69**, 122 (2012).
- [41] J. M. Burt, E. Josyula, and I. D. Boyd, *J. Thermophys. Heat Transfer* **26**, 258 (2012).
- [42] W. Jin, J. R. Ommen, and C. R. Kleijn, *Comput. Phys. Commun.* **212**, 146 (2017).
- [43] S. Shrestha, S. Tiwari, A. Klar, and S. Hardt, *J. Comput. Phys.* **292**, 239 (2015).
- [44] T. Baier, S. Tiwari, S. Shrestha, A. Klar, and S. Hardt, *Phys. Rev. Fluids* **3**, 094202 (2018).
- [45] A. K. Chinnappan, R. Kumar, V. K. Arghode, and R. S. Myong, *Phys. Fluids* **31**, 037104 (2019).
- [46] I. N. Ivchenko, S. K. Loyalka, and R. V. Tompson, Jr., *Analytical Methods for Problems of Molecular Transport, Fluid Mechanics and Its Applications* (Springer, Amsterdam, 2007).
- [47] S. Tao, H. Zhang, and Z. Guo, *J. Aerosol Sci.* **103**, 105 (2017).
- [48] G. Di Staso, H. J. H. Clercx, S. Succi, and F. Toschi, *J. Comput. Sci.* **17**, 357 (2016).
- [49] S. J. Plimpton, S. G. Moore, and A. Borner, *Phys. Fluids* **31**, 086101 (2019).
- [50] J. Happel and H. Brenner, *Low Reynolds Number Hydrodynamics* (Prentice-Hall, Englewood Cliffs, NJ, 1965).
- [51] E. Haines and T. Akenine-Möller, *Real-Time Rendering* (AK Peters, Natick, MA, 2002).
- [52] A. L. Garcia, *Numerical Methods for Physics (2nd Edition)* (Prentice-Hall, Englewood Cliffs, NJ, 1999).

- [53] S. Takata, Y. Sone, and K. Aoki, *Phys. Fluids A* **5**, 716 (1993).
- [54] G. Di Staso, Hybrid discretizations of the Boltzmann equation for the dilute gas flow regime, Ph.D. thesis, Eindhoven University of Technology, 2018.
- [55] R. Ouchene, M. Khalij, B. Arcen, and A. Taniere, *Powder Technol.* **303**, 33 (2016).
- [56] É. Guazzelli, J. F. Morris, and S. Pic, *A Physical Introduction to Suspension Dynamics*, Cambridge Texts in Applied Mathematics (Cambridge University Press, Cambridge, U.K., 2011).
- [57] L. Schiller and A. Z. Naumann, *Z. Ver. Deutsch. Ing.* **77**, 318 (1935).

Correction: A minor error in Eq. (18) has been fixed. An incorrect value given in the last entry of the fourth column of Table II has been replaced.